Inorganic Chemistry

pubs.acs.org/IC

Article

Functional Upgrading of an Organo−Ir(III) Complex to an Organo−Ir(III) Prodrug as a DNA Damage-Responsive Autophagic Inducer for Hypoxic Lung Cancer Therapy

Meng-Meng Wang,[§] Dong-Ping Deng,[§] An-Min Zhou,[§] Yan Su,* Zheng-Hong Yu,* Hong Ke Liu, and Zhi Su*

Cite This: *Inorg. Chem.* 2024, 63, 4758−4769

Read Online

ACCESS | Metrics & More | Article Recommendations | Supporting Information

ABSTRACT: The efficiency of nitrogen mustards (NMs), among the first chemotherapeutic agents against cancer, is limited by their monotonous mechanism of action (MoA). And tumor hypoxia is a significant obstacle in the attenuation of the chemotherapeutic efficacy. To repurpose the drug and combat hypoxia, herein, we constructed an organo−Ir(III) prodrug, **IrCpNM**, with the composition of a reactive oxygen species (ROS)-inducing moiety (Ir−arene fragment)−a hypoxic responsive moiety (azo linker)−a DNA-alkylating moiety (nitrogen mustard), and realized DNA damage response (DDR)-mediated autophagy for hypoxic lung cancer therapy for the first time. Prodrug **IrCpNM** could upregulate the level of catalase (CAT) to catalyze the decomposition of excessive H_2O_2 to O_2 and downregulate the expression of the hypoxia-inducible factor (HIF-1α) to relieve hypoxia. Subsequently, **IrCpNM** initiates the quadruple synergetic actions under hypoxia, as simultaneous ROS promotion and glutathione (GSH) depletion to enhance the redox disbalance and severe oxidative and cross-linking DNA damages to trigger the occurrence of DDR-mediated autophagy via the ATM/Chk2 cascade and the PIK3CA/PI3K-AKT1-mTOR-RPS6KB1 signaling pathway. In vitro and in vivo experiments have confirmed the greatly antiproliferative capacity of **IrCpNM** against the hypoxic solid tumor. This work demonstrated the effectiveness of the DNA damage-responsive organometallic prodrug strategy with the microenvironment targeting system and the rebirth of traditional chemotherapeutic agents with a new anticancer mechanism.

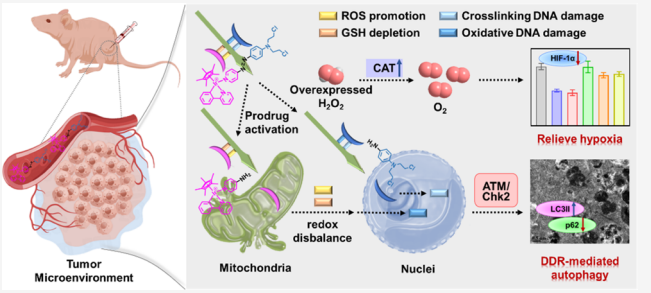

INTRODUCTION

The hypoxic microenvironment, as the major feature of the tumor microenvironment (TME), increased the resistance of cancer cells to the traditional chemotherapeutic treatments and attenuated the therapeutic effectiveness.[1,2] To resolve the problem of tumor hypoxia, O_2 self-sufficient systems were most desired to supply extra O_2, such as the utilization of overexpressed H_2O_2 in the TME to produce O_2.[3−5] However, even the overexpression of H_2O_2 was found in hypoxic cancer cells, the manipulation of endogenous enzymes to catalyze the decomposition of H_2O_2 to produce O_2 to relieve the hypoxic condition was still a huge challenge.[6,7] On the other hand, azoreductase was highly expressed in the hypoxic tumors, which could reductively cleave the azo bonds.[8,9] For example, many nanodrugs were designed with an azo-containing system as the outer shell for hypoxic cancer treatment, followed by the release of the internal active anticancer agents.[10] However, the nanosystem was usually very complicated with three or four independent components, which was a time-consuming work and the exact mechanism was hard to explain. In this case, small molecular anticancer agents with the capacity to overcome the hypoxic environment would still be the best choice.[11,12]

Metal−arene complexes, with the common formula of $[(Cp^x)M(L\text{^}L')Z]^{0/n+}$ (Cp^x, the arene caps; M, metal ions; L∧L′, chelated ligands; Z, the leaving groups), were first reported by Sadler and group as the potential anticancer agents (Scheme 1a).[13,14] Emerging evidence has revealed that the anticancer mechanisms for the oragnometallic complexes were distinct from classical *cis*-Pt through DNA damage-mediated apoptosis.[15] The typical Ir−arene complex, Ir(Cp*)(ppy)py (Cp*, pentamethylcyclopentadienyl; ppy, 2-phenylpyridine; py, pyridine), could result in the mitochondria-relevant damages as elevation of reactive oxygen species (ROS) and loss of the mitochondrial membrane potential (MMP).[16]

Received: January 6, 2024
Revised: February 4, 2024
Accepted: February 8, 2024
Published: February 26, 2024

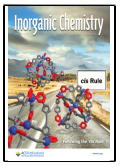

https://doi.org/10.1021/acs.inorgchem.4c00060
Inorg. Chem. 2024, 63, 4758−4769

Scheme 1. Schematic Illustration of the Anticancer Mechanism for the Multifunctional Prodrug IrCpNM: (a) Reported Classical Organo−Iridium Anticancer Agents, (b) Illustration of the Modification of the Small Molecular Prodrug Strategy, and (c) Design of IrCpNM and the Activation by Azoreductase

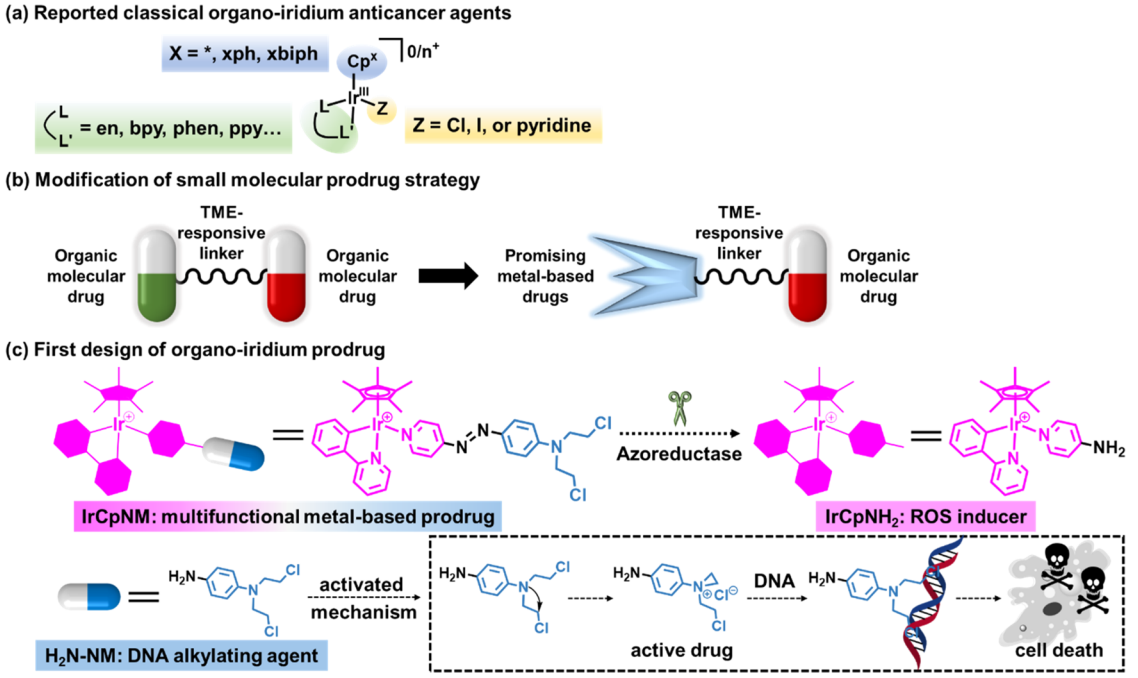

However, the underlying molecular mechanism has remained unclear. Moreover, new cell death pathways apart from apoptosis are urgent to be developed to bypass the flexible TME repellence of tumor cells. The alkylating agents bearing the $N(CH_2CH_2Cl)_2$ moiety, commonly known as 'the nitrogen mustards (NMs)', are among the early chemotherapeutic agents against cancer. They exert their biological functions by forming covalent alkyl linkages due to reaction with nucleophilic entities, viz., N^7 of guanine in DNA, which led to the impairment of DNA replication and transcription.[17] However, the single component of the Ir−arene complex or nitrogen mustard lost their antiproliferative capacity under hypoxia, which suggested that both anticancer mechanisms were highly dependent on the concentration of oxygen.

To minimize the hypoxic influence, the small molecular prodrug strategy was adopted to overcome the limitations of single-agent therapy,[18] which was applied for the first time for the metal−arene anticancer agent (Scheme 1b). The hypoxic azoreductase-responsive azo bond was considered and the new double halberd molecular **IrCpNM** was synthesized, with the construction of the ROS-inducing moiety (Ir−arene fragment)−the hypoxic reductase-responsive moiety (azo linker)−the DNA-alkylating moiety (nitrogen mustard) (Scheme 1c). **IrCpNM** exhibited superior cytotoxicity to A549 cells under hypoxia (1% O_2) with the IC_{50} value of 6 μM and comparative selectivity to cancer cells. The hypoxia has been significantly relieved due to the self-provided O_2 from the decomposition of H_2O_2 with the upregulated catalase activity and downregulated HIF-1α after **IrCpNM** treatment. **IrCpNM** could accumulate in the subcellular mitochondria and nuclei, and it could induce the quadruple synergetic actions, as simultaneous ROS elevation and glutathione (GSH) consumption to enhance the redox disbalance and severely oxidative and covalently cross-linking DNA damages to initiate DNA damage response (DDR)-mediated autophagy. DDR was driven by the ATM/Chk2 cascade (ataxia-telangiectasia-mutated/checkpoint kinase 2) and triggered by the DNA double-strand breaks (DSBs). The cell death mode for **IrCpNM**-treated A549 cells was DDR-mediated autophagy, which was first found for the metal-based anticancer agent and regulated by the PIK3CA/PI3K-AKT1-mTOR-RPS6KB1 signaling pathway. Both in vitro and in vivo biological experiments confirmed the greatly antiproliferative capacity of the complex **IrCpNM**. This work not only provided the example of the successful small molecular prodrug strategy in metal−arene anticancer agents but also demonstrated the effectiveness of the DNA damage-responsive organometallic prodrug strategy with the tumor microenvironment targeting system. Furthermore, this work offered a new insight for the rebirth of traditional chemotherapeutic agents with a new anticancer mechanism through rational design.

RESULTS AND DISCUSSION

Design, Syntheses, and Characterization. Complexes **IrCpNM** and **IrCpNH$_2$** were synthesized according to the previous literature methods with minor modifications (shown in Scheme S1).[16] In short, the precursor Ir(Cp*)(ppy)Cl reacted with the azo-containing ligand or 4-aminopyridine to form complexes **IrCpNM** and **IrCpNH$_2$**, respectively. The obtained complexes were fully characterized by ^{1}H NMR, ^{13}C NMR, elemental analysis (EA), ESI-HRMS, and HPLC (Figures S1−S16). The HPLC spectra of **IrCpNM** were also conducted at pH = 7 solution for 24 h, which indicated that **IrCpNM** owned relatively high stability and remained the same after 24 h standing in the dark condition (Figure S17). The UV−vis absorption spectra of **IrCpNM** has indicated that the complex **IrCpNM** could be stable in the presence of various biological species, such as cysteine, homocysteine, etc. (Figure S18a−g). However, the obvious interaction between the complex **IrCpNM** and the antioxidant glutathione (GSH) has been observed, as the absorption intensity of **IrCpNM**

https://doi.org/10.1021/acs.inorgchem.4c00060
Inorg. Chem. 2024, 63, 4758−4769

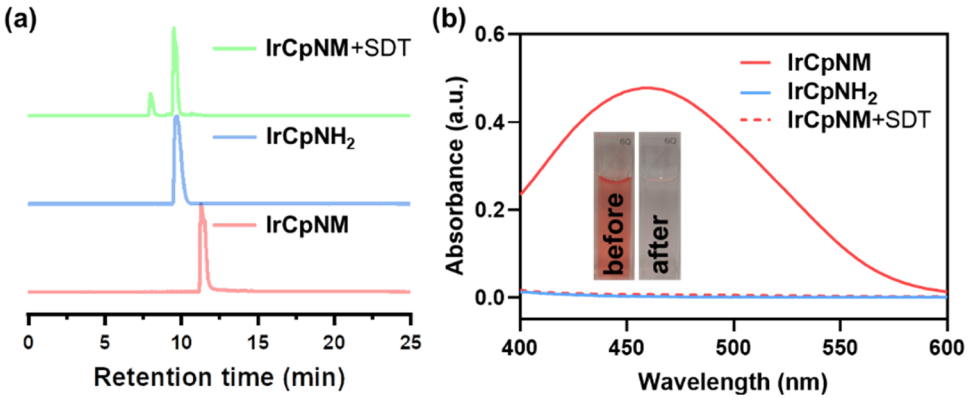

Figure 1. Extracellular reponse to the mimic of azoreductase SDT. (a) LC traces and (b) UV−vis spectra of **IrCpNM**, **IrCpNH$_2$**, and **IrCpNM** (20 μM) in the presence of SDT (2 mM, pH 7.4 at 310 K) for 30 min. Gradient: 20% B to 95% B in 25 min, then 80% A for 5 min (A: water with 0.1% formic acid, B: CH_3OH with 0.1% formic acid).

Table 1. IC_{50} Values of (μM) of IrCpNM, IrCpNH$_2$, NM, Mixture, and *cis*-Pt toward A549, A549R, and HLF Cell Lines after 48 h Treatment under Normoxia (20% O_2) and Hypoxia (1% O_2), Respectively[a]

complexes	IrCpNM	IrCpNH$_2$	NM	mixture[b]	*cis*-Pt
			normoxia (20% O_2)		
A549	1.7 ± 0.2	8.1 ± 0.9	72.4 ± 4.6	9.7 ± 0.5	9.2 ± 0.6
A549R	8.0 ± 1.5	19.5 ± 3.0	>100	22.3 ± 2.5	38.1 ± 1.5
HLF	12.7 ± 0.4	43.3 ± 0.3	158 ± 4.6	42.2 ± 2.7	4.9 ± 1.3
SI[c]	7.5	5.4	2.2	4.4	0.5
			hypoxia (1% O_2)		
A549	5.6 ± 0.4	26.9 ± 1.9	118 ± 14	37.6 ± 0.8	10.7 ± 0.9
A549R	31.9 ± 2.9	51.6 ± 4.8	>200	56.4 ± 2.7	47.1 ± 2.2
SI[c]	2.3	1.6	1.3	1.1	0.5

[a]Data are shown as the mean ± standard deviation (S.D., n = 3). [b]Mixture means the physical mixture of IrCpNH$_2$ and NM with the ratio of 1:1. [c]Cancer selectivity index (SI) is defined as the ratio of IC_{50} (HLF) in normoxia/IC_{50} (A549) in normoxia or hypoxia, respectively.

dropped in a concentration-dependent manner with the addition of GSH (Figure S18h). With the decoration of nitrogen mustard, the lipophilicity (log $P_{o/w}$) of **IrCpNM** was elevated to 2.37, compared to 0.04 of the complex **IrCpNH$_2$** (Table S1), suggesting that **IrCpNM** could be easier to enter cells than **IrCpNH$_2$** and would benefit its bioapplication.[19]

Interaction with DNA. Both fragments Ir−arene and nitrogen mustard were reported with the capacity to interact with DNA;[16,20] thereby, the binding constants of **IrCpNM** and **IrCpNH$_2$** to dsDNA were then calculated from the titration experiment,[21] as 2.2 × 10^4 and 4.2 × 10^4, respectively (Figure S19). Further, an in vitro DNA cleavage experiment was carried out on the supercoiled pBR322 plasmid using agarose gel (Figure S20). Cisplatin, as the DNA cross-linking agent, exhibited an outstanding capability of binding to pBR322 plasmid DNA (Figure S20b,c). The small molecular nitrogen mustard could bind to DNA under the low concentration (50 μM, Figure S20c), and it damaged the DNA into small species that smeared all over the gel at a high concentration (100 μM, Figure S20b). The complex **IrCpNM** could induce the conformational transition from the supercoiled plasmid to open-circular, as well as the linear plasmid in a concentration-dependent manner, while the complex **IrCpNH$_2$** indicated no obvious phenomenon under the same condition (Figure S20). These results elucidated that the complex **IrCpNM** was capable of inducing DNA damage.

Extracellular Response to SDT. Due to the existence of the azo group in **IrCpNM**, the response to azoreductase has been first evaluated under the hypoxia environment. Sodium dithionite (SDT), as a chemical mimic of azoreductase, was applied,[9] and the reduction process was observed by liquid chromatography mass spectrometry (LC-MS) (Figures 1a and S21). Complexes **IrCpNM** and **IrCpNH$_2$** owned the retention times of 11.43 and 9.75 min with the m/z values of 804.3 and 576.3, respectively (Figures 1a and S21). In the presence of SDT, the complex **IrCpNM** was completely disappeared and two new peaks with the retention times of 9.75 and 8.03 min were observed with the m/z values of 576.3 and 560.2, respectively, which could be assigned to the species of $[Ir(Cp^*)(ppy)(4\text{-aminopyridine})]^+$ and $[Ir(Cp^*)(ppy)(pyridine)]^+$. The activation of **IrCpNM** by SDT was further demonstrated by UV−vis spectra, where the pink color of the **IrCpNM** solution immediately changed to colorless after the addition of SDT (Figure 1b). These results suggested that the prodrug **IrCpNM** could be activated by azoreductase inside cancer cells under hypoxia to release the active fragments of Ir−arene and nitrogen mustard.

Cytotoxicity Assessment. The cytotoxicity of **IrCpNM** and **IrCpNH$_2$** was then assessed on human nonsmall cell lung cancer A549 cells, its cisplatin-resistant variant A549R cells, human breast cancer cell lines MCF-7 and MDA-MB-231, and human normal embryo-lung fibroblasts (HLFs) by MTT assay under both normoxia (20% O_2) and hypoxia (1% O_2) conditions (Tables 1 and S2). Compared to the control sample, the number of A549 cells was obviously decreased and the morphology apparently changed after 24 h exposure of **IrCpNM** under the hypoxia condition (Figure S22), suggesting that the complex **IrCpNM** could effectively inhibit the

https://doi.org/10.1021/acs.inorgchem.4c00060
Inorg. Chem. 2024, 63, 4758−4769

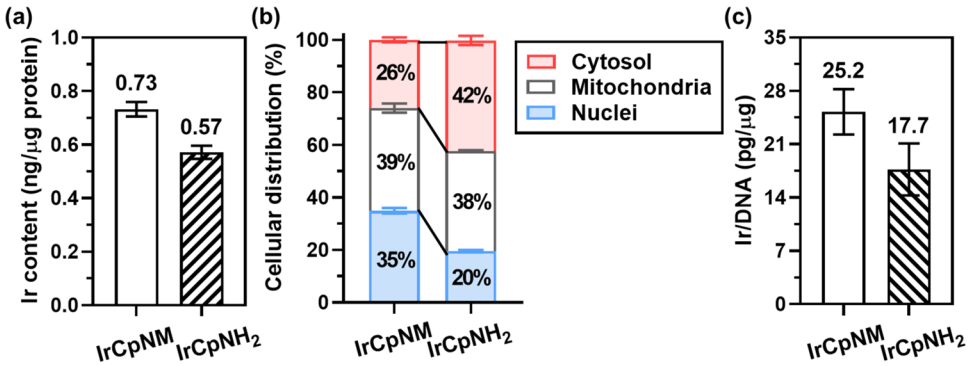

Figure 2. Intracellular uptake and distribution of **IrCpNM** and **IrCpNH$_2$** in A549 cells under hypoxia. (a) Cellular uptake (ng/μg protein) and (b) intracellular distribution of Ir in A549 cells after incubation with **IrCpNM** or **IrCpNH$_2$** (10 μM) for 6 h at 310 K under hypoxia. (c) Ir content of genomic DNA in A549 cells after treatment with **IrCpNM** and **IrCpNH$_2$** (5 μM) for 24 h at 310 K under hypoxia (n = 3). Error bars: S.D., n = 3.

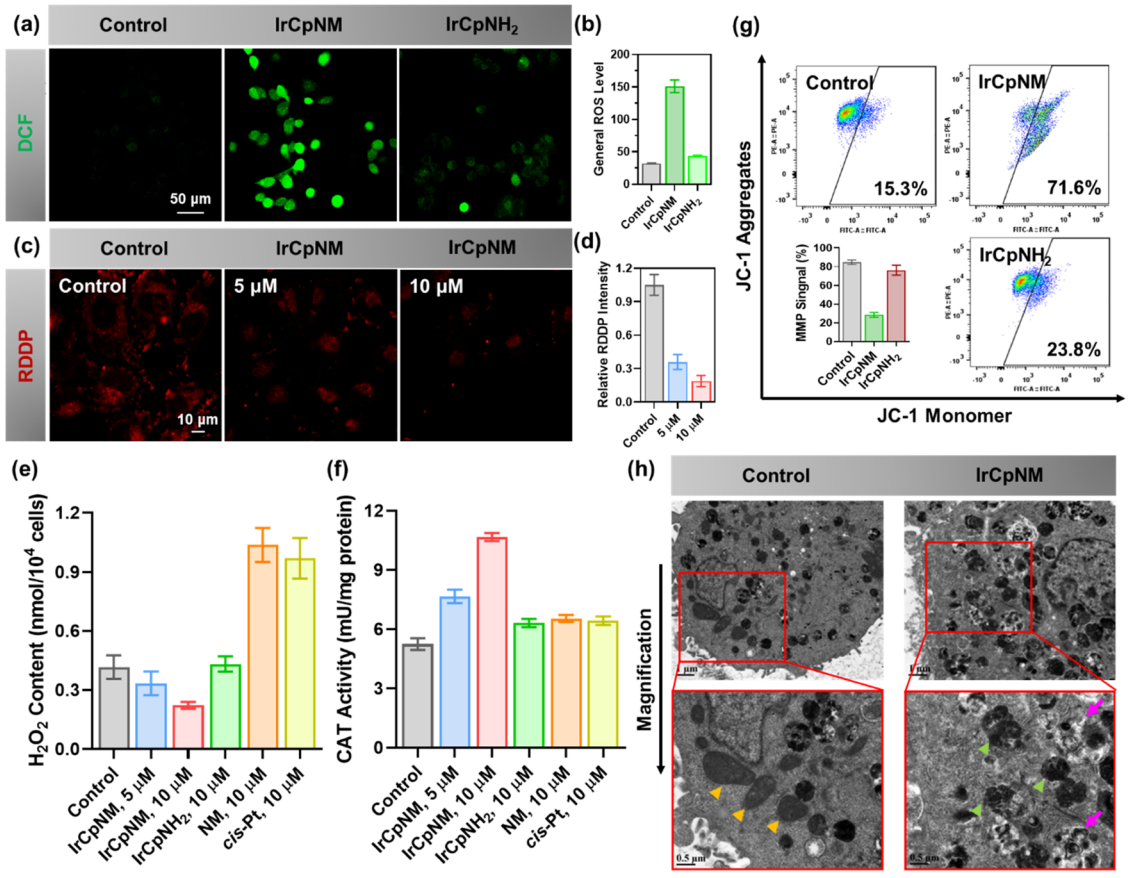

Figure 3. Oxidative stress and self-supplied O_2 in **IrCpNM**-treated A549 cells under hypoxia. (a) Confocal images and (b) quantitative flow cytometry results of the overall ROS level stained with DCF (10 μM) for 30 min in A549 cells treated with **IrCpNM** and **IrCpNH$_2$** (10 μM) for 24 h at 310 K under hypoxia. (c) Confocal images of O_2 content pretreatment with RDDP dye (5 μM) for 4 h in A549 cells then treated with **IrCpNM** (5, 10 μM) for 24 h at 310 K under hypoxia and (d) quantitative results of RDDP intensity in panel (c) inversely proportional to O_2 content. (e) H_2O_2 content and (f) CAT activity in A549 cells after the indicated complex treatments (5 and 10 μM for **IrCpNM** and 10 μM for **IrCpNH$_2$**, NM and *cis*-Pt) for 24 h at 310 K under hypoxia. (g) Flow cytometry quantification of the MMP labeled with JC-1 (5 μg/mL) for 30 min in A549 cells treated with **IrCpNM** and **IrCpNH$_2$** (10 μM) for 24 h at 310 K under hypoxia. Error bars: S.D., n = 3. (h) Representative TEM images of the mitochondrial morphology and autophagic process in A549 cells treated with **IrCpNM** (10 μM) for 24 h at 310 K under hypoxia. The orange, green, and pink arrows represented the healthy mitochondria, damaged mitochondria, and autolysosome, respectively.

proliferation of A549 cells. Nitrogen mustard (NM) could be regarded as nontoxic (IC_{50} > 110 μM) under hypoxia. **IrCpNM** indicated a much better antiproliferative performance than **IrCpNH$_2$** and the mixture to A549 cells under hypoxia, where the IC_{50} value of **IrCpNM** (6 μM) was much lower than those of **IrCpNH$_2$** (27 μM) and the mixture (38 μM). Furthermore, **IrCpNM** indicated the best antiproliferative performance to A549 cells, among the tested cancer lines. The mixture exhibited even less cytotoxicity than that of **IrCpNH$_2$**, suggesting that free NM hardly contributed to the cytotoxicity and even antagonized **IrCpNH$_2$**. This phenomenon was also found for the mixture of cisplatin with naproxen.[22] The

https://doi.org/10.1021/acs.inorgchem.4c00060
Inorg. Chem. 2024, 63, 4758−4769

cytotoxicity indicated that the linkage of the Ir−arene fragment with NM by the azo group could generate the synergetic effect to enhance the anticancer performance.

Moreover, the complex **IrCpNM** showed much less cytotoxicity to normal HLF cells than to A549 cells with the selectivity index (SI) of 2.3/7.5 under the hypoxia/normoxia conditions, respectively (Table 1), which indicated that **IrCpNM** could attenuate the side effects from the treatment comparing to cisplatin (SI value of 0.5).[23] Even the IC_{50} value for **IrCpNM** to A549 cells under hypoxia (6 μM) was higher than that under normoxia (2 μM). **IrCpNM** still exhibited a promising anticancer efficiency under hypoxia. According to previous reports, the hypoxia-inducible factor (HIF-1α), as the marker for the hypoxic condition of cells, would be dramatically overexpressed under hypoxia.[24] Western blotting demonstrated that the expression of HIF-1α in A549 cells under hypoxia was downregulated after **IrCpNM** treatment, suggesting that the hypoxia was effectively relieved (Figure S23).

Intracellular Accumulation and Distribution. The intracellular uptakes and distributions of **IrCpNM** and **$IrCpNH_2$** were examined by inductively coupled plasma mass spectrometry (ICP-MS). The cellular Ir content for **IrCpNM** is 0.73 ng/μg protein, about a 1.3-fold elevation to 0.57 ng/μg protein for **$IrCpNH_2$** (Figure 2a and Table S3), which is ascribed to the better lipophilicity of **IrCpNM**.[25] In contrast to the complex **$IrCpNH_2$**, an obvious increased accumulation of **IrCpNM** in the nuclei was observed from 20 to 35%, which was due to the existence of nitrogen mustard. The accumulation in the mitochondria was similar for both **IrCpNM** (39%) and **$IrCpNH_2$** (38%), which suggested that the Ir−arene fragment owned a strong mitochondria-targeting capacity (Figure 2b and Table S3). Considering the similar DNA-binding affinity, the binding capacities of **IrCpNM** and **$IrCpNH_2$** to genomic DNA of A549 cells were then examined. After treatments, the genomic DNA in A549 cells was extracted and the quantity of binding Ir content was measured by ICP-MS. About 40% elevation of DNA-binding Ir content was found for the complex **IrCpNM** (25.2 pg/μg) compared to that of **$IrCpNH_2$** (17.7 pg/μg) (Figure 2c). This suggested that the elevated DNA-binding content of **IrCpNM** mainly resulted from a higher intracellular uptake.

ROS Elevation and Mitochondrial Damage. The impact of **IrCpNM** treatment under hypoxia on the mitochondria was first evaluated since approximately 40% of **IrCpNM** accumulated in the mitochondria. Mitochondria is the main site for ROS generation,[26] and the overall intracellular ROS production was probed with 2′,7′-dichlorofluorescin diacetate (DCF-DA) fluorescence assay by flow cytometry and confocal laser scanning microscopy (CLSM). A dramatic concentration-dependent ROS elevation was observed in **IrCpNM**-treated A549 cells, which has been elevated 4.7-fold compared to the control sample with the concentration of 10 μM (Figures 3a,b and S24). Meanwhile, the complex **$IrCpNH_2$**, as expected, showed a concentration-dependent ROS production under hypoxia (Figure S25), while the ROS production in the presence of 10 μM **$IrCpNH_2$** was much less than that of **IrCpNM** (Figures 3a,b and S24). This implied that the ROS elevation in **IrCpNM**-treated A549 cells was ascribed to the mitochondrial damage.

To demonstrate the endogenous O_2 generation in A549 cells to relieve the hypoxia, $[Ru(dpp)_3]Cl_2$ (RDDP), as the oxygen indicator,[27] was incubated with the **IrCpNM**-treated A549 cells, where the fluorescence of RDDP could be quenched by O_2. The red fluorescence intensity has been significantly attenuated in a dose-dependent manner after **IrCpNM** treatment, suggesting that the O_2 content has been obviously elevated in the **IrCpNM**-treated A549 cells (Figure 3c,d).

Furthermore, H_2O_2 could be the resource of endogenous O_2 and decomposed to O_2 and H_2O by catalase (CAT);[6,28] thus, the H_2O_2 content and CAT activity in A549 cells were then examined after **IrCpNM** treatment (Figure 3e−f). The results demonstrated that the H_2O_2 content has been dramatically consumed (Figure 3e) and CAT activity has been significantly promoted in a dose-dependent manner after **IrCpNM** treatment (Figure 3f), which further confirmed that O_2 could be self-provided from the decomposition of overexpressed H_2O_2 by the elevated CAT activity. This self-provided O_2 could relieve the hypoxia and attenuate the expression of HIF-1α.

The massive ROS production under hypoxia would trigger a series of mitochondrial damages.[29] Mitochondrial Ca^{2+} homeostasis was highly related to the permeability of the mitochondrial membrane, and the Ca^{2+} overload would promote the opening of the mitochondrial permeability transition pore (mPTP), eventually leading to the loss of the mitochondrial membrane potential (MMP).[30] A free Ca^{2+} fluorescence probe, Fluo-4 AM, was used to monitor the intracellular Ca^{2+} content, and an obvious green fluorescence was observed in the 10 μM **IrCpNM**-treated A549 cells (Figure S26). Furthermore, the loss of the MMP was also demonstrated with the observation of CLSM and flow cytometry. **IrCpNM**-treated A549 cells emitted a strong green fluorescence with the mitochondria-selective aggregate dye JC-1 and the depolarized mitochondria jump from 15.3% (control sample) to 71.6% with 10 μM **IrCpNM** (Figures 3g and S27). These results suggested that **IrCpNM** could induce the mitochondrial Ca^{2+} overload and loss of the MMP under hypoxia.

The integration of the mitochondria is essential to maintain the physiological functions,[31] and mitochondrial morphology was then examined by transmission electron microscopy (TEM). The mitochondria in the untreated A549 cells owned a clear-outlined mitochondrial double-layer membrane and the cristae structure (Figure 3h, orange arrowheads). In contrast, vacuolation containing intracellular contents was observed after **IrCpNM** treatment (Figure 3h, pink arrows), and most of the mitochondrial cristae structures were destroyed or disappeared (Figure 3h, green arrowheads), indicating that the mitochondria were severely damaged and autophagic cell death would be initiated.

Disruption of Redox Homeostasis. Since excessive ROS production under hypoxia was observed in **IrCpNM**-treated A549 cells, the redox homeostasis of cells must be disrupted. Glutathione (GSH), as the primary endogenous antioxidant in cells, could protect cancer cells from oxidative stress to perform normal physiological activities. Intracellular GSH could be oxidized to oxidized glutathione (GSSG) by the direct interaction with radicals or by glutathione peroxidases (GPx) during the reduction of hydrogen peroxide. Meanwhile, GSSG would be simultaneously reduced back to GSH by nicotinamide adenine dinucleotide phosphate (NADPH) with the catalyst of glutathione reductase (GR) to maintain redox homeostasis, where the NADPH was oxidized to $NADP^+$.[4,28]

As expected, after **IrCpNM** treatment, the contents of GSH and GSSG in A549 cells have been simultaneously down- and

https://doi.org/10.1021/acs.inorgchem.4c00060
Inorg. Chem. 2024, 63, 4758−4769

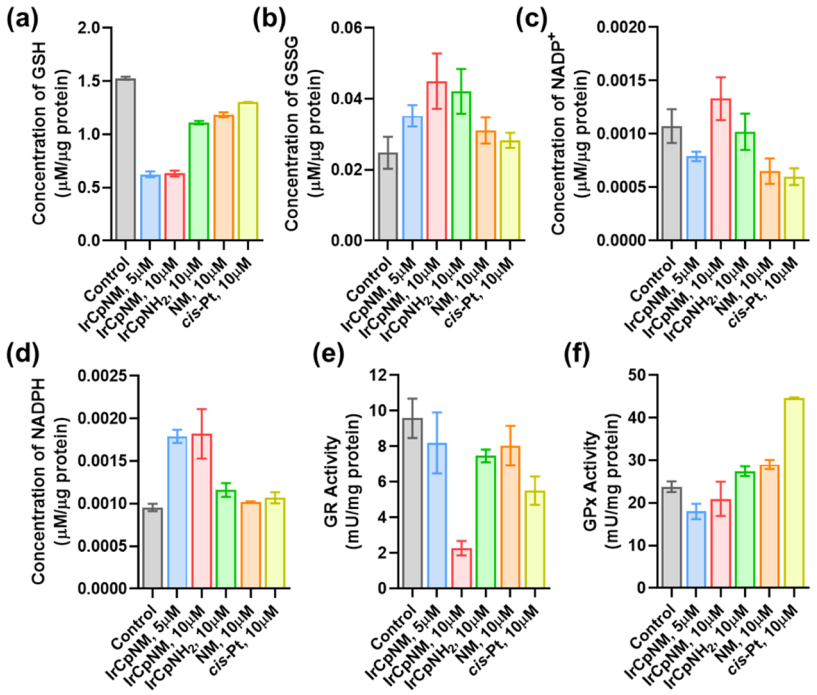

Figure 4. Disruption of GSH homeostasis in **IrCpNM**-treated A549 cells under hypoxia. (a–d) Concentration of GSH, GSSG, $NADP^+$, and NADPH (μM/μg protein) and (e, f) GR and GPx activities (mU/mg protein) in A549 cells treated with indicated complexes (5 and 10 μM for **IrCpNM** and 10 μM for $\mathbf{IrCpNH_2}$, NM and *cis*-Pt) for 24 h at 310 K under hypoxia. Error bars: S.D., $n = 3$.

upregulated, respectively (Figure 4a,b). And the expression of GPx was also elevated in a concentration-dependent manner, which promoted the transformation from GSH to GSSG (Figure 4f). In addition, even the levels of NADPH and $NADP^+$ upregulated after **IrCpNM** treatment, the enzyme activity of GR has been dramatically inhibited (Figure 4c–e). Even the GR activity was suppressed in a concentration-dependent manner in the presence of **IrCpNM**; the GSH content remains the same. This may be due to the complexity of the cellular environment, where the GSH content has been determined by many factors other than GR activity, such as the level of cysteine.[32] These results indicated that the disruption of redox homeostasis was mainly ascribed to the limited reduction of GSSG to GSH, resulting in excessive ROS production.

Initiation of DNA Damage. γ-H2AX (the phosphorylated form of the histone protein H2AX), as the biomarker of DNA double-strand breaks (DSBs),[22,33] was then examined. As is known, NM and *cis*-Pt are the alkylating agents of DNA, and γ-H2AX expression in NM- and *cis*-Pt-treated A549 cells was significantly elevated as well as the cisplatin-treated cells (Figure 5b). It is worthy to note that γ-H2AX expression in **IrCpNM**-treated A549 cells was 1.4 and 1.6 times higher compared to those in NM- and *cis*-Pt-treated cells, respectively (Figure 5b,c), which suggested that **IrCpNM** could induce more serious DNA damage than NM. Furthermore, the immunofluorescence intensity of γ-H2AX foci was also dramatically enhanced in **IrCpNM**-treated A549 cells, suggesting that **IrCpNM** treatment strengthened the frequency of DNA double-strand breaks (Figure S28).[34] In addition, alkaline comet assay revealed that the DNA double helix has been partially denatured and some nuclear DNA has become single-stranded after **IrCpNM** treatment (Figure 5a).[35]

In order to detect whether DNA damage was also mediated by oxidative stress (OS) from the excessive ROS production,[36] γ-H2AX expression of A549 cells in the presence of the antioxidant ROS inhibitor NAC was further examined (Figure 5d,e). The immunoblotting result indicated that the expression level of γ-H2AX was significantly inhibited by 33% with the addition of NAC, illustrating that DNA damage in the **IrCpNM**-treated A549 cells partially resulted from oxidative stress. Thus, **IrCpNM** could simultaneously initiate the cross-linking and oxidative DNA damage in A549 cells.

DNA Damage Response-Mediated Autophagy through the ATM/Chk2 Cascade and the PIK3CA/PI3K-AKT1-mTOR-RPS6KB1 Pathway. DNA damage could trigger various cellular responses, such as DNA repair, cell cycle arrest, apoptosis, necrosis, and autophagy.[37,38] As reported, DNA damage response (DDR) could be driven by two major pathways, the ataxia-telangiectasia-mutated/checkpoint kinase 2 (ATM/Chk2) and the ATM- and RAD3-related serine/threonine kinase (ATR/Chk1) signaling cascade, respectively.[39,40] The ATM/Chk2 pathway could be activated by DSBs, whereas ATR/Chk1 signaling was usually activated by single-strand breaks (SSBs) or bulky DNA lesions. The phosphorylation levels of Chk1 and Chk2 in the **IrCpNM**-treated A549 cells were evaluated by immunoblotting assay (Figure 5f). In contrast to both upregulated expressions in cisplatin-treated A549 cells, only Chk2 phosphorylation has been obviously increased by 50 and 98% with different concentrations of **IrCpNM** treatment (Figure 5f,g), suggesting that the major mode of DNA damage was DSBs, which was consistent with the observation from γ-H2AX expression and the comet assay.

The expression of p53, as a downstream effector of DNA damage,[33,41] has been studied and the results indicated that p53 expression was severely elevated in the **IrCpNM**-treated A549 cells (Figure 5b,c), indicating that DNA damage could not be repaired and the cell death process could be initiated. The analysis of cell cycle distribution and dual staining of

https://doi.org/10.1021/acs.inorgchem.4c00060
Inorg. Chem. 2024, 63, 4758–4769

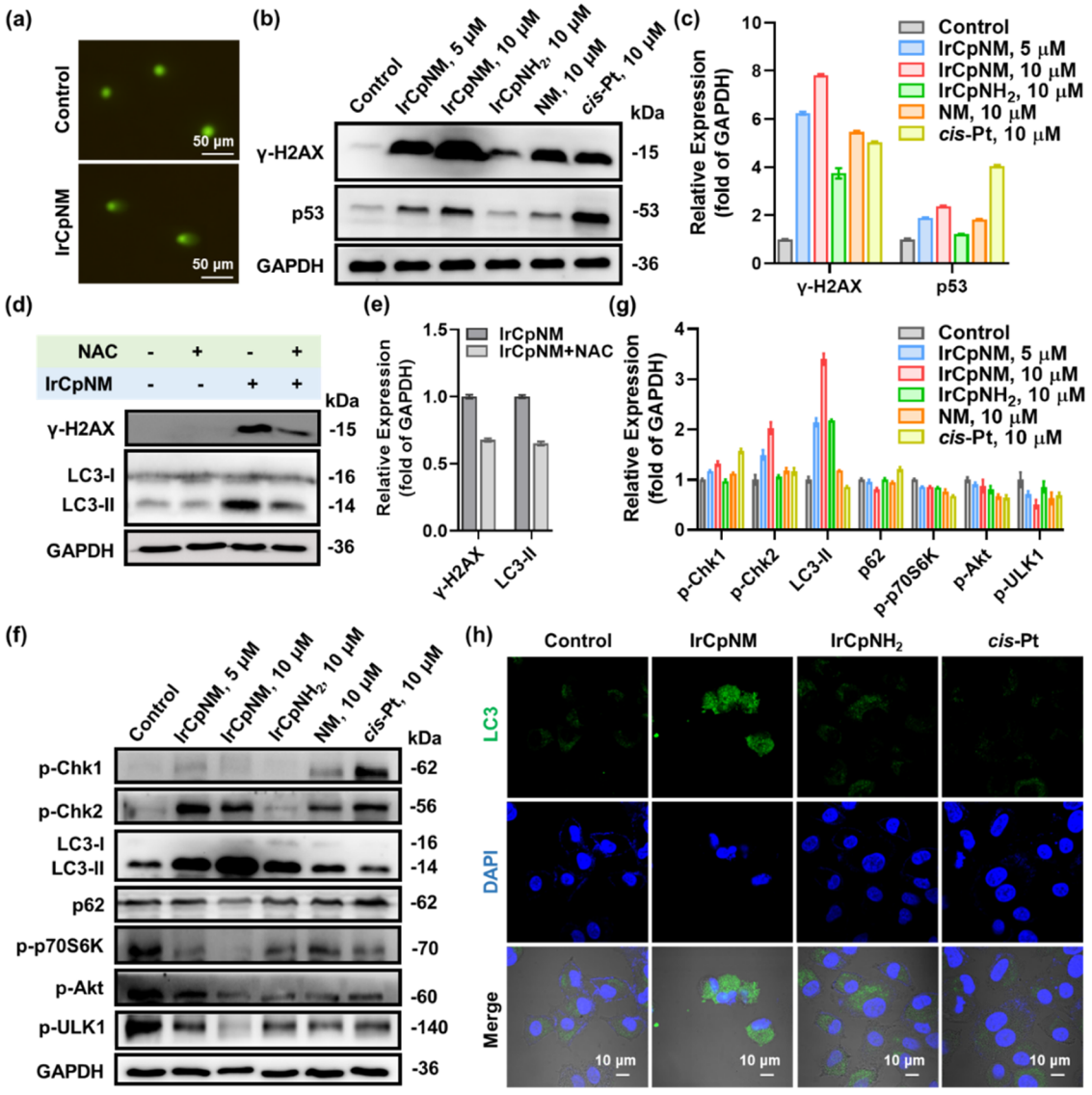

Figure 5. DDR-mediated autophagy in 24 h **IrCpNM**-treated A549 cells through the ATM/CHK2 pathway under hypoxia. (a) Comet assay of A549 cells treated with **IrCpNM** (10 μM) for 24 h at 310 K under hypoxia. (b) Expression level of γ-H2AX and p53 in A549 cells treated with indicated complexes (5 and 10 μM for **IrCpNM** and 10 μM for **IrCpNH$_2$**, NM and *cis*-Pt) for 24 h at 310 K under hypoxia. (c) The corresponding protein contents in panel (b) relative to GAPDH. (d) Expression level of γ-H2AX and LC3 with or without the preincubation of NAC (2.5 mM) for 1 h in A549 cells then treated with or without **IrCpNM** (10 μM) for 24 h at 310 K under hypoxia. (e) The corresponding protein contents in panel (d) relative to GAPDH. (f) Expression level of proteins involved in DDR-mediated autophagy signaling pathways in A549 cells treated with indicated complexes (5 and 10 μM for **IrCpNM** and 10 μM for **IrCpNH$_2$**, NM and *cis*-Pt) for 24 h at 310 K under hypoxia. (g) The corresponding protein contents in panel (f) relative to GAPDH. (h) Immunofluorescence staining of LC3 in A549 cells treated with **IrCpNM**, **IrCpNH$_2$**, and *cis*-Pt (10 μM) for 24 h at 310 K under hypoxia.

Annexin V-FITC and PI assay illustrated that **IrCpNM** could not induce cell cycle arrest and trigger apoptosis in A549 cells (Figure S29a,b). Furthermore, the cell viability was not elevated with the presence of several inhibitors, including z-VAD-fmk, necrostatin-1 (Nec-1), or ferrostatin-1 (Fer-1), suggesting that the cell death did not result from apoptosis, necrosis, or ferroptosis after **IrCpNM** treatment (Figure S30). In contrast, 3-methyladenine (3-MA) and chloroquine, the most-used autophagy inhibitor, could elevate the cell viability, which suggested that autophagy was the predominant death mode of the **IrCpNM**-treated A549 cells (Figure S31).

The expression of the autophagy-related protein light chain protein 3 (LC3) was then examined to confirm the occurrence of autophagy by immunofluorescence and immunoblotting (Figure 5f–h). The conversion from LC3-I (microtubule-associated protein 1 light chain 3) to its lipidation form LC3-II, a reliable marker of autophagy,[42] was initiated after **IrCpNM** treatment in a concentration-dependent manner (Figure 5f,g). The apparently increased fluorescence intensity was also observed in the **IrCpNM**-treated A549 cells (Figure 5h). Furthermore, the p62 expression level was also downregulated in the **IrCpNM**-treated A549 cells, which would degrade with the autophagosomes to complete the autophagic flux (Figure 5f,g).[43] These results confirmed the occurrence of DNA damage response-mediated autophagy in the **IrCpNM**-treated A549 cells.

It is well known that the signaling pathway of phosphatidylinositol-4,5-bisphosphate 3-kinase, catalytic subunit α

https://doi.org/10.1021/acs.inorgchem.4c00060
Inorg. Chem. 2024, 63, 4758−4769

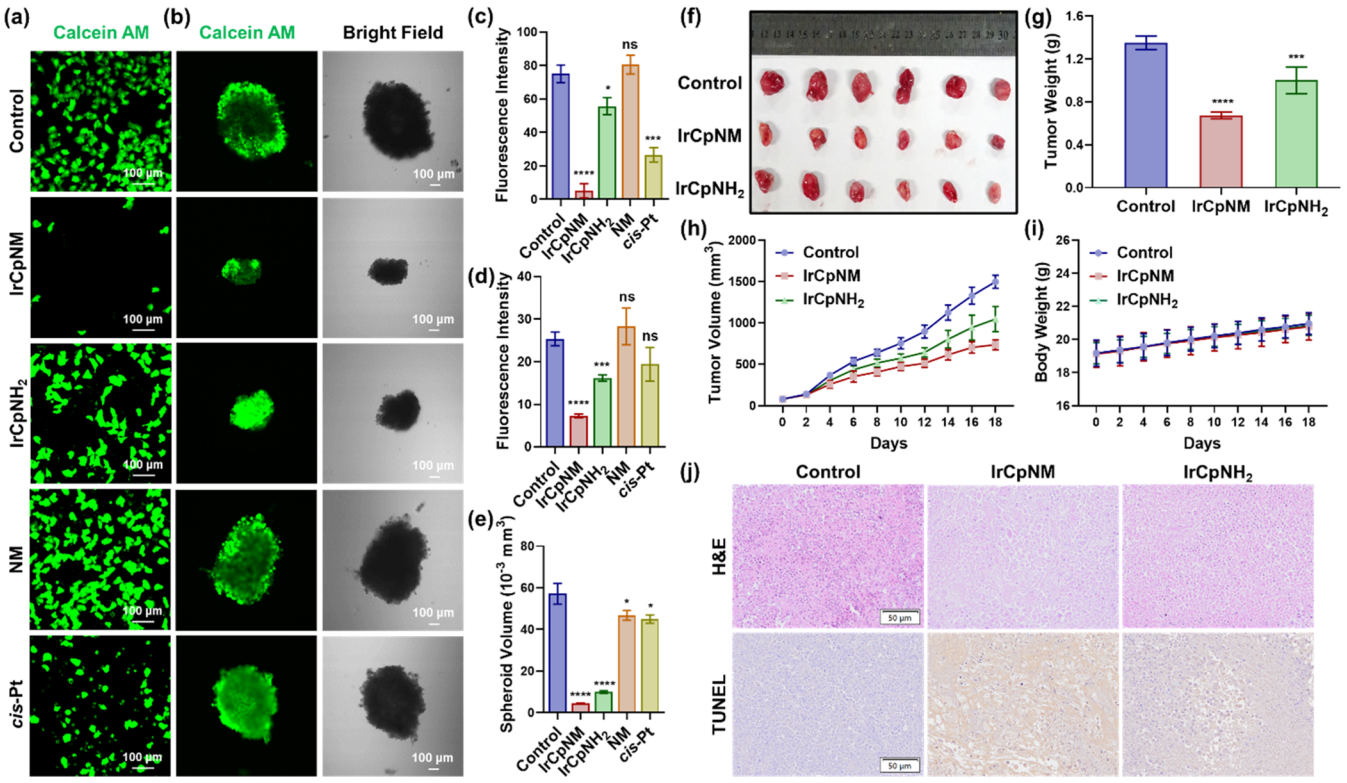

Figure 6. Antiproliferation of **IrCpNM** on the different biological models. (a) 2D A549 monolayer cells after treatment with **IrCpNM**, **IrCpNH$_2$**, NM, and *cis*-Pt (10 μM) for 24 h at 310 K under hypoxia and (b) 3D A549 tumor spheroids after treatment with **IrCpNM**, **IrCpNH$_2$**, NM, and *cis*-Pt (20 μM) for 7 days. (c, d) Statistical fluorescence intensity of calcein AM in panels (a) and (b), respectively, and (e) volume of 3D tumor spheroids in panel (b). (f, g) Representative photographs and the weight of tumor samples (n = 6) after treatment with saline, **IrCpNM**, and **IrCpNH$_2$** (5.0 mg kg^{-1} of body weight) for 18 days, respectively. *p < 0.05, ***p < 0.001, ****p < 0.0005. (h, i) Time-dependent tumor growth curves and the body weight of the mice during 18 days. Error bars: S.D., n = 6. (j) H&E and TUNEL staining assays of tumor tissues at the end of the indicated treatment.

(PIK3CA/PI3K)-v-akt murine thymoma viral oncogene homologue 1 (AKT1)- mechanistic target of rapamycin (mTOR)- ribosomal protein S6 kinase, 70 kDa, polypeptide 1 (RPS6KB1) could regulate the occurrence of autophagy in cells.[44] To further demonstrate the inhibition of the PIK3CA/PI3K-AKT1-MTOR-RPS6KB1 pathway to induce autophagy in the **IrCpNM**-treated A549 cells, the expression of the related proteins was further examined by Western blotting (Figure 5f,g). After treatment with **IrCpNM** for 24 h, an obvious suppression of phosphorylated AKT1 (p-Akt) at ser473 and phosphorylated RPS6KB1 (p-p70S6K) at thr389 in a concentration-dependent manner was observed compared to the untreated A549 cells (Figure 5f,g). Furthermore, the initiation of autophagy was also coordinated with unc-51-like kinase 1 (ULK1, also known as autophagy-related (ATG)-1), which could be inhibited by mTOR.[38] The Western blotting results showed that phosphorylated ULK1 (p-ULK1) at ser757 was suppressed in a concentration-dependent manner in **IrCpNM**-treated A549 cells (Figure 5f,g). Moreover, in the presence of NAC, autophagy was also inhibited, as the ratio of LC3-II/LC3-I was decreased (Figure 5d,e). This suggested that DNA damage response-mediated autophagy regulated by the PIK3CA/PI3K-AKT1-mTOR-RPS6KB1 signaling pathway resulted from both the cross-linking and oxidative DNA damages, which provided a new anticancer mechanism for the metal−arene anticancer agents.

Biological Evaluation In Vitro and In Vivo. The antiproliferative performance of both complexes **IrCpNM** and **IrCpNH$_2$** was then evaluated in three biological models, as the 2D monolayer cells, the 3D multicellular tumor spheroids (MCTSs), and the A549 tumor-bearing mice models.[45] As shown in Figure 6a,6c, nearly no green fluorescence was observed after 24 h **IrCpNM** treatment, suggesting that the complex **IrCpNM** killed most of the A549 cells and exhibited the greatest antiproliferative effect toward A549 cells among complexes **IrCpNH$_2$**, NM, and cisplatin.

3D tumor spheroids of A549 cells were cultured to mimic the microenvironment of the solid tumor with an average diameter of 500 μm and were treated with complexes **IrCpNM** and **IrCpNH$_2$**, respectively (Figures 6b,d−e and S32). After 7 days incubation with **IrCpNM**, the spheroid volume shrunk to only 10% of the control sample (Figure 6e). In contrast, the spheroids treated with NM and cisplatin showed very limited influence on the proliferation of A549 spheroids.

Inspired by the in vitro study, the in vivo antitumor performance of **IrCpNM** and **IrCpNH$_2$** in A549 tumor-bearing mice models was further evaluated (Figures 6f−j and S33). The tumor-bearing mice were randomly divided into three groups (6 mice/group) and intratumorally injected with **IrCpNM** or **IrCpNH$_2$** (5 mg kg^{-1} mice weight) or saline once every other day for 18 days. The growth of the tumors was significantly inhibited after **IrCpNM** treatment compared to the control and the **IrCpNH$_2$**-treated group. The average tumor volumes for the **IrCpNM**- and **IrCpNH$_2$**-treated groups were 737.1 and 1047.0 mm^3, respectively. The control group was characterized with a rapid growth of the tumor volume up

https://doi.org/10.1021/acs.inorgchem.4c00060
Inorg. Chem. 2024, 63, 4758−4769

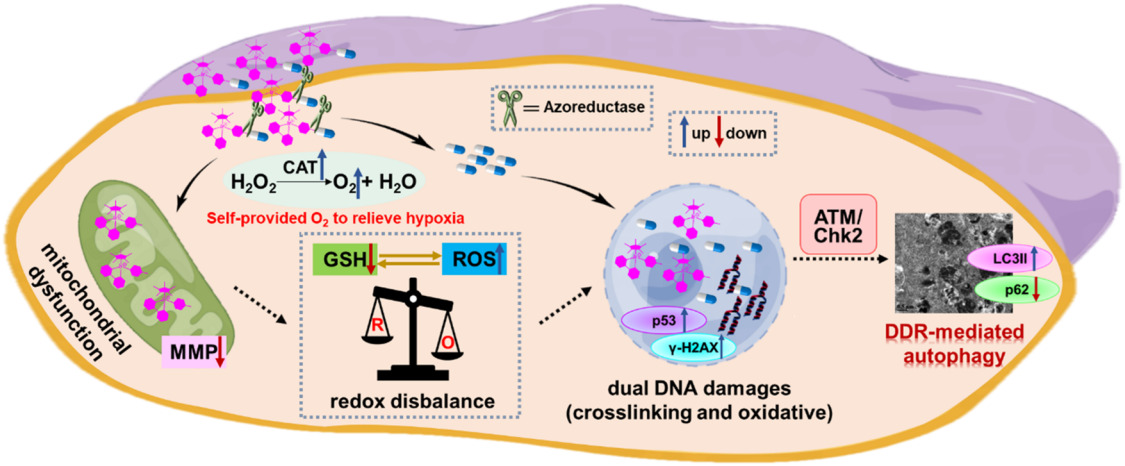

Figure 7. Proposed mechanism of action for **IrCpNM**.

to 1498.1 mm^3 (Figure 6f,6h). Meanwhile, the tumor weight of the **IrCpNM**-treated group was the lowest compared to the other groups (Figure 6g). In addition, the body weight of the mice treated with **IrCpNM** or **IrCpNH$_2$** showed no obvious difference to the control group during the treatment, as the steady growth (Figure 6i), which indicated that **IrCpNM** owned potent antitumor activity in vivo and low toxicity to the mice.

Hematoxylin and eosin (H&E) staining and terminal deoxynucleotidyl transferase dUTP nick-end labeling (TUNEL) staining assays were also performed to evaluate the therapeutic efficacy of the different treatments (Figures 6j and S33). The images of the H&E and TUNEL-stained tumor tissue showed that **IrCpNM** induced a high level of cell death in the mice (Figure 6j). However, the control group showed no obvious tumor necrosis. Notably, no apparent lesions of the major organs were observed in mice treated with **IrCpNM** or **IrCpNH$_2$** (Figure S33), indicating the minimal adverse effects and the excellent biocompatibility of **IrCpNM**.

Mechanism of Action. Emerging studies have revealed that DNA binding does not appear to be the major antitumor mechanism of current organo−iridium complexes. Instead, increase of ROS and loss of MMP might significantly contribute to their anticancer activities.[16] Here, we demonstrate that the organo−iridium prodrug, upon triggering the occurrence of ROS storms, can subsequently induce a cascade of physiological responses in tumor cells, including redox imbalance and DNA oxidative damage, ultimately leading to the activation of DDR-mediated autophagy for hypoxic lung cancer therapy. The overall antitumor mechanism of **IrCpNM** is depicted in Figure 7. Specifically, this prodrug can respond to overexpressed azoreductase under hypoxia, thereby ameliorating the hypoxic tumor environment through self-provided O_2 from the decomposition of H_2O_2 with upregulated catalase activity and downregulated HIF-1α. Consequently, the Ir−arene and nitrogen mustard fragments can accumulate in the subcellular mitochondria and nuclei, inducing the quadruple synergetic actions, including simultaneous ROS promotion and GSH depletion leading to redox disbalance, and oxidative and cross-linking DNA damages to initiate DDR-mediated autophagy through the ATM/Chk2 cascade and the PIK3CA/PI3K-AKT1-mTOR-RPS6KB1 pathway.

CONCLUSIONS

In this work, considering the tumor hypoxia microenvironment and the monotonous mechanism of exiting drugs, an azoreductase-responsive multifunctional complex **IrCpNM** was designed and successfully synthesized. The organo−Ir(III) prodrug **IrCpNM** was constructed with the ROS-inducing moiety−the azoreductase-responsive moiety−the DNA alkylating moiety, which could initiate the quadruple synergetic actions in A549 cells. The hypoxia has been significantly relieved due to downregulated HIF-1α and the self-provided O_2 from the decomposition of H_2O_2 with upregulated catalase activity by **IrCpNM**. The Ir−arene fragment could promote the elevation of ROS; the azo bond could be simultaneously reduced by azoreductase and GSH to enhance the disbalance of redox homeostasis, resulting in the occurrence of oxidative DNA damage; nitrogen mustard could covalently link to DNA, resulting in cross-linking DNA damage. Both oxidative and cross-linking DNA damage triggered the DDR by the ATM/Chk2 cascade with the DNA double-strand breaks. DDR-mediated autophagy was subsequently regulated by the PIK3CA/PI3K-AKT1-mTOR-RPS6KB1 signaling pathway, which was a new anticancer mechanism for the metal-based anticancer agents. This work not only provided the example of the successful small molecular prodrug strategy for metal−arene agents to resolve the hypoxic obstacle but also demonstrated the effectiveness of the DNA damage response strategy with the tumor microenvironment targeting system. Moreover, this work offered a new insight for the rebirth of traditional chemotherapeutic agents with a new anticancer mechanism through rational design.

EXPERIMENTAL SECTION

Chemicals and Reagents. $[Ir(Cp^*)_2Cl]_2$ (Cp^* = tetramethyl cyclopentadienyl), ppy (2-phenylpyridine), 4-aminopyridine, and NH_4PF_6 were purchased from Heowns. *N*,*N*-Bis(2-chloroethyl)aniline was obtained from Macklin. All commercial chemicals and reagents for syntheses were of analytical grade and used as received without further purification. Deuterated solvents for NMR purposes were obtained from Merck and Cambridge Isotopes.

Synthesis of the Ligand (L). The ligand (*E*)-*N*,*N*-bis(2-chloroethyl)-4-(pyridin-4-yldiazenyl)aniline (L) was synthesized from the coupling of 4-aminopyridine and nitrogen mustard (NM) in a slightly modified way according to

https://doi.org/10.1021/acs.inorgchem.4c00060
Inorg. Chem. 2024, 63, 4758−4769

literature procedures.[46] Briefly, to a stirred solution of 4-aminopyridine (1.5 mmol, 141 mg) in a mixture solvent of ACN/H_2O (1:1, v/v) at 273 K under an argon atmosphere, $NaNO_2$ (1.6 mmol, 110 mg) was added and the solution was stirred for 10 min, after which concentrated HCl (6 mmol, 0.5 mL) was added and the solution was stirred for another 30 min. Subsequently, NM (1 mmol, 218 mg) in ACN was added dropwise and the mixture was stirred for 3 h at 273 K, after which 100 mL of water was added. The mixture was extracted with DCM (3 × 50 mL), the organic layers were combined and dried over with $MgSO_4$, and the solvent was removed in vacuo. The crude product was purified by silica gel chromatography eluted with petroleum ether/ethyl acetate (10:1, v/v) to give the pure L. Yield: 150 mg (43%). ^{1}H NMR (400 MHz, $CDCl_3$) δ (ppm): 8.96−8.59 (m, 2H), 8.08−7.85 (m, 2H), 7.78−7.57 (m, 2H), 6.93−6.67 (m, 2H), 3.89 (t, J = 6.9 Hz, 4H), 3.73 (t, J = 6.9 Hz, 4H). ^{13}C NMR (101 MHz, $CDCl_3$) δ (ppm): 157.73, 151.04, 149.70, 144.50, 126.21, 116.15, 111.64, 53.46, 40.18. ESI-MS (CH_3OH): calcd for $[C_{15}H_{16}Cl_2N_4]^+$ m/z = 323.08, found m/z = 323.10.

Synthesis of Complexes (IrCpNM and IrCpNH$_2$). The iridium precursor Ir(Cp*)(ppy)Cl was synthesized and purified as previously reported.[47] The complexes **IrCpNM** and **IrCpNH$_2$** were prepared by the similar method following the reference.[16] Generally, a solution of the chloride complex Ir(Cp*)(ppy)Cl (0.1 mmol, 51.8 mg) and $AgNO_3$ (1 mol equiv) in MeOH/H_2O (1:1, v/v) was refluxed in the dark under an argon atmosphere for 3 h. Then, the precipitate (AgCl) was removed by filtration, and the ligand L or 4-aminopyridine (1 mol equiv) was added to the filtrate. The reaction mixture was refluxed under an argon atmosphere overnight, which was then exchanged with NH_4PF_6 (10 mol equiv).

[Ir(Cp*)(ppy)(L)]PF$_6$ (IrCpNM). The crude product was purified by silica gel chromatography eluted with *n*-hexane/ethyl acetate (10:1, v/v) to give the pure product. The complex **IrCpNM** was obtained as a red powder. Yield: 0.056 g (59%). ^{1}H NMR (400 MHz, $CDCl_3$) δ (ppm): 9.15 (d, J = 5.7 Hz, 1H), 8.53−8.47 (m, 2H), 7.94 (dd, J = 7.6, 1.1 Hz, 1H), 7.81 (td, J = 7.0, 2.8 Hz, 4H), 7.67−7.60 (m, 2H), 7.57−7.51 (m, 2H), 7.41 (td, J = 7.5, 1.3 Hz, 1H), 7.19 (td, J = 7.5, 1.1 Hz, 1H), 6.76−6.69 (m, 2H), 3.87 (t, J = 6.8 Hz, 4H), 3.71 (t, J = 6.7 Hz, 4H), 1.65 (s, 15H). ^{13}C NMR (101 MHz, $CDCl_3$) δ (ppm): 166.76, 160.82, 158.20, 154.19, 152.19, 150.80, 145.35, 144.49, 138.99, 134.81, 132.00, 126.99, 125.30, 124.33, 123.91, 119.23, 119.17, 111.77, 90.47, 53.41, 40.30, 8.56. Elemental analysis: calcd (%) for $C_{36}H_{39}Cl_2F_6IrN_5P$: C, 45.52; H, 4.14; N, 7.37; found: C, 45.66; H, 4.27; N, 7.21. ESI-MS (CH_3OH): calcd for [**IrCpNM** - PF_6^-]$^+$ m/z = 804.2, found m/z = 804.3. ESI-HRMS (CH_3OH): calcd for [**IrCpNM** - PF_6^-]$^+$ m/z = 804.2212, found m/z = 804.2159.

[Ir(Cp*)(ppy)(4-aminopyridine)]PF$_6$ (IrCpNH$_2$). The pure product of **IrCpNH$_2$** was obtained by recrystallizing from dichloromethane/diethyl ether. The complex **IrCpNH$_2$** was obtained as a yellow powder. Yield: 0.061 g (85%). ^{1}H NMR (400 MHz, d_6-DMSO) δ (ppm): 8.94 (dd, J = 5.8, 1.5 Hz, 1H), 8.15 (d, J = 8.1 Hz, 1H), 7.99 (td, J = 7.8, 1.5 Hz, 1H), 7.89 (dd, J = 7.6, 1.1 Hz, 1H), 7.85 (dd, J = 7.9, 1.4 Hz, 1H), 7.65−7.56 (m, 2H), 7.49 (ddd, J = 7.3, 5.7, 1.4 Hz, 1H), 7.34 (td, J = 7.4, 1.4 Hz, 1H), 7.13 (td, J = 7.5, 1.1 Hz, 1H), 6.78 (s, 2H), 6.34−6.23 (m, 2H), 1.56 (s, 15H). ^{13}C NMR (101 MHz, $CDCl_3$) δ (ppm): 167.17, 161.34, 154.37, 151.50, 151.17, 145.03, 138.69, 134.61, 131.87, 124.47, 124.36, 123.58, 119.39, 111.85, 89.81, 8.55. Elemental analysis: calcd (%) for $C_{26}H_{29}F_6IrN_3P$: C, 43.33; H, 4.06; N, 5.83; found: C, 43.51; H, 4.21; N, 5.63. ESI-MS (CH_3OH): calcd for [**IrCpNH$_2$** - PF_6^-]$^+$ m/z = 576.2, found m/z = 576.3. ESI-HRMS (CH_3OH): calcd for [**IrCpNH$_2$** - PF_6^-]$^+$ m/z = 576.1991, found m/z = 576.1977.

■ ASSOCIATED CONTENT

Supporting Information

The Supporting Information is available free of charge at https://pubs.acs.org/doi/10.1021/acs.inorgchem.4c00060.

Materials and experimental details and the NMR, ESI-MS, confocal images, and flow cytometry results for complexes **IrCpNM** and **IrCpNH$_2$** (PDF)

■ AUTHOR INFORMATION

Corresponding Authors

Yan Su − *Jiangsu Collaborative Innovation Center of Biomedical Functional Materials, College of Chemistry and Materials Science, Nanjing Normal University, Nanjing 210023, China; Department of Rheumatology and Immunology, Jinling Hospital, Medical School of Nanjing University, Nanjing 210002, China*; Email: suyanahnu@163.com

Zheng-Hong Yu − *Department of Rheumatology and Immunology, Jinling Hospital, Medical School of Nanjing University, Nanjing 210002, China*; Email: m_fish@189.cn

Zhi Su − *Jiangsu Collaborative Innovation Center of Biomedical Functional Materials, College of Chemistry and Materials Science, Nanjing Normal University, Nanjing 210023, China*; orcid.org/0000-0002-1339-0525; Email: zhisu@njnu.edu.cn

Authors

Meng-Meng Wang − *Jiangsu Collaborative Innovation Center of Biomedical Functional Materials, College of Chemistry and Materials Science, Nanjing Normal University, Nanjing 210023, China*

Dong-Ping Deng − *Jiangsu Collaborative Innovation Center of Biomedical Functional Materials, College of Chemistry and Materials Science, Nanjing Normal University, Nanjing 210023, China*

An-Min Zhou − *Jiangsu Collaborative Innovation Center of Biomedical Functional Materials, College of Chemistry and Materials Science, Nanjing Normal University, Nanjing 210023, China*

Hong Ke Liu − *Jiangsu Collaborative Innovation Center of Biomedical Functional Materials, College of Chemistry and Materials Science, Nanjing Normal University, Nanjing 210023, China*

Complete contact information is available at: https://pubs.acs.org/10.1021/acs.inorgchem.4c00060

Author Contributions

§M.-M.W., D.-P.D., and A.-M.Z. contributed equally.

Notes

The authors declare no competing financial interest.

■ ACKNOWLEDGMENTS

The authors appreciate the financial support from the National Natural Science Foundation of China (NSFC) (grant nos. 21977052 and 22277056) and the Distinguished Young

Scholars of Jiangsu Province (SBK2023010017). Y.S. was supported by the Jiangsu Excellent Postdoctoral Program and NSF of Jiangsu Province (BK2023040369).

REFERENCES

(1) Singleton, D. C.; Macann, A.; Wilson, W. R. Therapeutic targeting of the hypoxic tumour microenvironment. *Nat. Rev. Clin. Oncol.* **2021**, *18*, 751−772.
(2) Harris, A. L. Hypoxia–a key regulatory factor in tumour growth. *Nat. Rev. Cancer* **2002**, *2*, 38−47.
(3) Wei, F. M.; Rees, T. W.; Liao, X. X.; Ji, L. N.; Chao, H. Oxygen self-sufficient photodynamic therapy. *Coord. Chem. Rev.* **2021**, *432*, No. 213714.
(4) Lu, N.; Deng, Z. H.; Gao, J.; Liang, C.; Xia, H. P.; Zhang, P. Y. An osmium-peroxo complex for photoactive therapy of hypoxic tumors. *Nat. Commun.* **2022**, *13*, No. 2245.
(5) Zhao, X. Z.; Liu, J. P.; Fan, J. L.; Chao, H.; Peng, X. J. Recent progress in photosensitizers for overcoming the challenges of photodynamic therapy: from molecular design to application. *Chem. Soc. Rev.* **2021**, *50*, 4185−4219.
(6) Yang, G. G.; Su, X. X.; Liang, B. B.; Pan, Z. Y.; Cao, Q.; Mao, Z. W. A platinum-ruthenium hybrid prodrug with multi-enzymatic activities for chemo-catalytic therapy of hypoxic tumors. *Chem. Sci.* **2022**, *13*, 11360−11367.
(7) Jiang, F.; Zhao, Y. J.; Yang, C. Z.; Cheng, Z. Y.; Liu, M.; Xing, B. G.; Ding, B. B.; Ma, P. A.; Lin, J. A tumor microenvironment-responsive Co/ZIF-8/ICG/Pt nanoplatform for chemodynamic and enhanced photodynamic antitumor therapy. *Dalton Trans.* **2022**, *51*, 2798−2804.
(8) Xue, T. H.; Shen, J. J.; Shao, K. C.; Wang, W.; Wu, B.; He, Y. N. Strategies for Tumor Hypoxia Imaging Based on Aggregation-Induced Emission Fluorogens. *Chem. −Eur. J.* **2020**, *26*, 2521−2528.
(9) Yuan, J.; Zhou, Q. H.; Xu, S.; Zuo, Q. P.; Li, W.; Zhang, X. X.; Ren, T. B.; Yuan, L.; Zhang, X. B. Enhancing the Release Efficiency of a Molecular Chemotherapeutic Prodrug by Photodynamic Therapy. *Angew. Chem.* **2022**, *61*, No. e202206169.
(10) Huang, C. X.; Tan, W. L.; Zheng, J.; Zhu, C.; Huo, J.; Yang, R. H. Azoreductase-Responsive Metal-Organic Framework-Based Nanodrug for Enhanced Cancer Therapy via Breaking Hypoxia-induced Chemoresistance. *ACS Appl. Mater. Interfaces* **2019**, *11*, 25740−25749.
(11) Kim, J. H.; Verwilst, P.; Won, M.; Lee, J.; Sessler, J. L.; Han, J.; Kim, J. S. A Small Molecule Strategy for Targeting Cancer Stem Cells in Hypoxic Microenvironments and Preventing Tumorigenesis. *J. Am. Chem. Soc.* **2021**, *143*, 14115−14124.
(12) Jung, H. S.; Han, J.; Shi, H.; Koo, S.; Singh, H.; Kim, H. J.; Sessler, J. L.; Lee, J. Y.; Kim, J. H.; Kim, J. S. Overcoming the Limits of Hypoxia in Photodynamic Therapy: A Carbonic Anhydrase IX-Targeted Approach. *J. Am. Chem. Soc.* **2017**, *139*, 7595−7602.
(13) Liu, Z.; Salassa, L.; Habtemariam, A.; Pizarro, A. M.; Clarkson, G. J.; Sadler, P. J. Contrasting reactivity and cancer cell cytotoxicity of isoelectronic organometallic iridium(III) complexes. *Inorg. Chem.* **2011**, *50*, 5777−5783.
(14) Liu, Z.; Sadler, P. J. Organoiridium complexes: anticancer agents and catalysts. *Acc. Chem. Res.* **2014**, *47*, 1174−1185.
(15) Hearn, J. M.; Canelón, I. R.; Qamar, B.; Liu, Z.; Portman, I. H.; Sadler, P. J. Organometallic Iridium(III) anticancer complexes with new mechanisms of action: NCI-60 screening, mitochondrial targeting, and apoptosis. *ACS Chem. Biol.* **2013**, *8*, 1335−1343.
(16) Liu, Z.; Canelón, I. R.; Abraha Habtemariam; Clarkson, G. J.; Sadler, P. J. Potent Half-Sandwich Iridium(III) Anticancer Complexes Containing C∧N-Chelated and Pyridine Ligands. *Organometallics* **2014**, *33*, 5324−5333.
(17) Singh, R. K.; Kumar, S.; Prasad, D. N.; Bhardwaj, T. R. Therapeutic journery of nitrogen mustard as alkylating anticancer agents: Historic to future perspectives. *Eur. J. Med. Chem.* **2018**, *151*, 401−433.
(18) Patel, T. K.; Adhikari, N.; Amin, S. A.; Biswas, S.; Jha, T.; Ghosh, B. Small molecule drug conjugates (SMDCs): an emerging strategy for anticancer drug design and discovery. *New J. Chem.* **2021**, *45*, 5291−5321.
(19) Karges, J.; Kuang, S.; Maschietto, F.; Blacque, O.; Ciofini, I.; Chao, H.; Gasser, G. Rationally designed ruthenium complexes for 1- and 2-photon photodynamic therapy. *Nat. Commun.* **2020**, *11*, No. 3262.
(20) Karmakar, S.; Maji, M.; Mukherjee, A. Modulation of the reactivity of nitrogen mustards by metal complexation: approaches to modify their therapeutic properties. *Dalton Trans.* **2019**, *48*, 1144−1160.
(21) Ling, Y. Y.; Xia, X. Y.; Hao, L.; Wang, W. J.; Zhang, H.; Liu, L. Y.; Liu, W. T.; Li, Z. Y.; Tan, C. P.; Mao, Z. W. Simultaneous Photoactivation of cGAS-STING Pathway and Pyroptosis by Pt(II)-Triphenylamine Complexes for Cancer Immunotherapy. *Angew. Chem., Int. Ed.* **2022**, *61* (43), No. e202210988, DOI: 10.1002/anie.202210988.
(22) Jin, S. X.; Muhammad, N.; Sun, Y. W.; Tan, Y. H.; Yuan, H.; Song, D. F.; Guo, Z. J.; Wang, X. Y. Multispecific Platinum(IV) Complex Deters Breast Cancer via Interposing Inflammation and Immunosuppression as an Inhibitor of COX-2 and PD-L1. *Angew. Chem.* **2020**, *132* (51), 23513−23521, DOI: 10.1002/anie.202011273.
(23) Wang, K.; Zhu, C. C.; He, Y. F.; Zhang, Z. Q.; Zhou, W.; Muhammad, N.; Guo, Y.; Wang, X. Y.; Guo, Z. J. Restraining Cancer Cells by Dual Metabolic Inhibition with a Mitochondrion-Targeted Platinum(II) Complex. *Angew. Chem., Int. Ed.* **2019**, *58*, 4638−4643.
(24) Su, X.; Wang, W. J.; Cao, Q.; Zhang, H.; Liu, B.; Ling, Y. Y.; Zhou, X. T.; Mao, Z. W. A Carbonic Anhydrase IX (CAIX)-Anchored Rhenium(I) Photosensitizer Evokes Pyroptosis for Enhanced Anti-Tumor Immunity. *Angew. Chem., Int. Ed.* **2022**, *61* (8), No. e202115800, DOI: 10.1002/anie.202115800.
(25) Wang, L.; Guan, R.; Xie, L.; Liao, X.; Xiong, K.; Rees, T. W.; Chen, Y.; Ji, L.; Chao, H. An ER-Targeting Iridium(III) Complex which Induces Immunogenic Cell Death in Non-Small Cell Lung Cancer. *Angew. Chem.* **2021**, *60*, 4707−4715, DOI: 10.1002/anie.202013987.
(26) Vyas, S.; Zaganjor, E.; Haigis, M. C. Mitochondria and Cancer. *Cell* **2016**, *166*, 555−566.
(27) Cao, Q.; Zhou, D. J.; Pan, Z. Y.; Yang, G. G.; Zhang, H.; Ji, L. N.; Mao, Z. W. CAIXplatins: Highly Potent Platinum(IV) Prodrugs Selective Against Carbonic Anhydrase IX for the Treatment of Hypoxic Tumors. *Angew. Chem., Int. Ed.* **2020**, *59*, 18556−18562.
(28) Wang, F. X.; Liang, J. H.; Zhang, H.; Wang, Z. H.; Wan, Q.; Tan, C. P.; Ji, L. N.; Mao, Z. W. Mitochondria-Accumulating Rhenium(I) Tricarbonyl Complexes Induce Cell Death via Irreversible Oxidative Stress and Glutathione Metabolism Disturbance. *ACS Appl. Mater. Interfaces* **2019**, *11*, 13123−13133.
(29) Kuang, S.; Sun, L. L.; Zhang, X. R.; Liao, X. X.; Rees, T. W.; Zeng, L. L.; Chen, Y.; Zhang, X. T.; Ji, L. N.; Chao, H. A Mitochondrion-Localized Two-Photon Photosensitizer Generating Carbon Radicals Against Hypoxic Tumors. *Angew. Chem., Int. Ed.* **2020**, *59*, 20697−20703.
(30) Wallace, D. C. Mitochondria and cancer. *Nat. Rev. Cancer* **2012**, *12*, 685−698.
(31) Wang, M. M.; Xu, F. J.; Su, Y.; Geng, Y.; Qian, X. T.; Xue, X. L.; Kong, Y. Q.; Yu, Z. H.; Liu, H. K.; Su, Z. A New Strategy to Fight Metallodrug Resistance: Mitochondria-Relevant Treatment through Mitophagy to Inhibit Metabolic Adaptations of Cancer Cells. *Angew. Chem., Int. Ed.* **2022**, *61*, No. e202203843, DOI: 10.1002/anie.202203843.
(32) Kennedy, L.; Sandhu, J. K.; Harper, M. E.; Cuperlovic Culf, M. Role of Glutathione in Cancer: From Mechanisms to Therapies. *Biomolecules* **2020**, *10*, 1429.
(33) Zhang, S. R.; Zhong, X. M.; Yuan, H.; Guo, Y.; Song, D. F.; Qi, F.; Zhu, Z. Z.; Wang, X. Y.; Guo, Z. J. Interfering in apoptosis and DNA repair of cancer cells to conquer cisplatin resistance by platinum(IV) prodrugs. *Chem. Sci.* **2020**, *11*, 3829−3835.

https://doi.org/10.1021/acs.inorgchem.4c00060
Inorg. Chem. 2024, 63, 4758−4769

(34) Su, Y.; Tu, Y.; Lin, H.; Wang, M. M.; Zhang, G. D.; Yang, J.; Liu, H. K.; Su, Z. Mitochondria-targeted Pt(IV) prodrugs conjugated with an aggregation-induced emission luminogen against breast cancer cells by dual modulation of apoptosis and autophagy inhibition. *J. Inorg. Biochem.* **2022**, *226*, No. 111653.
(35) Xue, X. L.; Fu, Y.; He, L.; Salassa, L.; He, L. F.; Hao, Y. Y.; Koh, M. J.; Soulie, C.; Needham, R. J.; Habtemariam, A.; Garino, C.; Lomachenko, K. A.; Su, Z.; Qian, Y.; Paterson, M. J.; Mao, Z. W.; Liu, H. K.; Sadler, P. J. Photoactivated Osmium Arene Anticancer Complexes. *Inorg. Chem.* **2021**, *60*, 17450−17461.
(36) Tian, Z. H.; Liu, H. H.; Chen, X. H.; Losiewicz, M. D.; Wang, R.; Du, X. D.; Wang, B. Q.; Ma, Y.; Zhang, S. Y.; Shi, L. J.; Guo, X.; Wang, Y. S.; Zhang, B. Y.; Yuan, S. M.; Zeng, X.; Zhang, H. Z. The activated ATM/p53 pathway promotes autophagy in response to oxidative stress-mediated DNA damage induced by Microcystin-LR in male germ cells. *Ecotoxicol. Environ. Saf.* **2021**, *227*, No. 112919, DOI: 10.1016/j.ecoenv.2021.112919.
(37) Liu, M. D.; Zeng, T. L.; Zhang, X.; Liu, C. Y.; Wu, Z. H.; Yao, L. M.; Xie, C. C.; Xia, H.; Lin, Q.; Xie, L. P.; Zhou, D. W.; Deng, X. M.; Chan, H. L.; Zhao, T. J.; Wang, H. R. ATR/Chk1 signaling induces autophagy through sumoylated RhoB-mediated lysosomal translocation of TSC2 after DNA damage. *Nat. Commun.* **2018**, *9*, No. 4139.
(38) Wang, W. J.; Li, J. S.; Tan, J. Y.; Wang, M. M.; Yang, J.; Zhang, Z. M.; Li, C. Z.; Basnakian, A. G.; Tang, H. W.; Perrimon, N.; Zhou, Q. H. Endonuclease G promotes autophagy by suppressing mTOR signaling and activating the DNA damage response. *Nat. Commun.* **2021**, *12*, No. 476.
(39) Jangili, P.; Kong, N.; Kim, J. H.; Zhou, J.; Liu, H.; Zhang, X.; Tao, W.; Kim, J. S. DNA-Damage-Response-Targeting Mitochondria-Activated Multifunctional Prodrug Strategy for Self-Defensive Tumor Therapy. *Angew. Chem., Int. Ed.* **2022**, *61* (16), No. e202117075, DOI: 10.1002/anie.202117075.
(40) O'Connor, M. J. Targeting the DNA Damage Response in Cancer. *Mol. Cell* **2015**, *60*, 547−560.
(41) Ge, C.; Di, X. J.; Han, S. Q.; Wang, M. M.; Qian, X. T.; Su, Z.; Liu, H. K.; Qian, Y. Hydrogen sulfide triggered molecular agent for imaging and cancer therapy. *Chem. Commun.* **2021**, *57*, 1931−1934.
(42) Xue, X. L.; Qian, C. G.; Tao, Q.; Dai, Y. X.; Lv, M. D.; Dong, J. W.; Su, Z.; Qian, Y.; Zhao, J.; Liu, H. K.; Guo, Z. J. Using Bioorthogonally Catalyzed Lethality Strategy to Generate Mitochondria-Targeting Antitumor Metallodrugs in vitro and in vivo. *Natl. Sci. Rev.* **2021**, *8*, No. nwaa286.
(43) Huang, Y. Y.; You, X.; Wang, L. N.; Zhang, G. X.; Gui, S. L.; Jin, Y. L.; Zhao, R.; Zhang, D. Q. Pyridinium-Substituted Tetraphenylethylenes Functionalized with Alkyl Chains as Autophagy Modulators for Cancer Therapy. *Angew. Chem., Int. Ed.* **2020**, *59*, 10042−10051.
(44) Guo, W. J.; Zhang, Y. M.; Zhang, L.; Huang, B.; Tao, F. F.; Chen, W.; Guo, Z. J.; Xu, Q.; Sun, Y. Novel monofunctional platinum (II) complex Mono-Pt induces apoptosis-independent autophagic cell death in human ovarian carcinoma cells, distinct from cisplatin. *Autophagy* **2013**, *9*, 996−1008.
(45) Su, Y.; Lin, H.; Tu, Y.; Wang, M. M.; Zhang, G. D.; Yang, J.; Liu, H. K.; Su, Z. Fighting metallodrug resistance through alteration of drug metabolism and blockage of autophagic flux by mitochondria-targeting AIEgens. *Chem. Sci.* **2022**, *13*, 1428−1439.
(46) Hu, M. X.; Yang, C.; Luo, Y.; Chen, F.; Yang, F. F.; Yang, S. P.; Chen, H.; Cheng, Z. Q.; Li, K.; Xie, Y. M. A hypoxia-specific and mitochondria-targeted anticancer theranostic agent with high selectivity for cancer cells. *J. Mater. Chem. B* **2018**, *6*, 2413−2416.
(47) Liu, Z.; Habtemariam, A.; Pizarro, A. M.; Clarkson, G. J.; Sadler, P. J. Organometallic Iridium(III) Cyclopentadienyl Anticancer Complexes Containing C,N-Chelating Ligands. *Organometallics* **2011**, *30*, 4702−4710.

https://doi.org/10.1021/acs.inorgchem.4c00060
Inorg. Chem. 2024, 63, 4758−4769